Journal of Materials Chemistry A

Accepted Manuscript

ROYAL SOCIETY OF CHEMISTRY

www.rsc.org/materialsA

Graphical Abstract

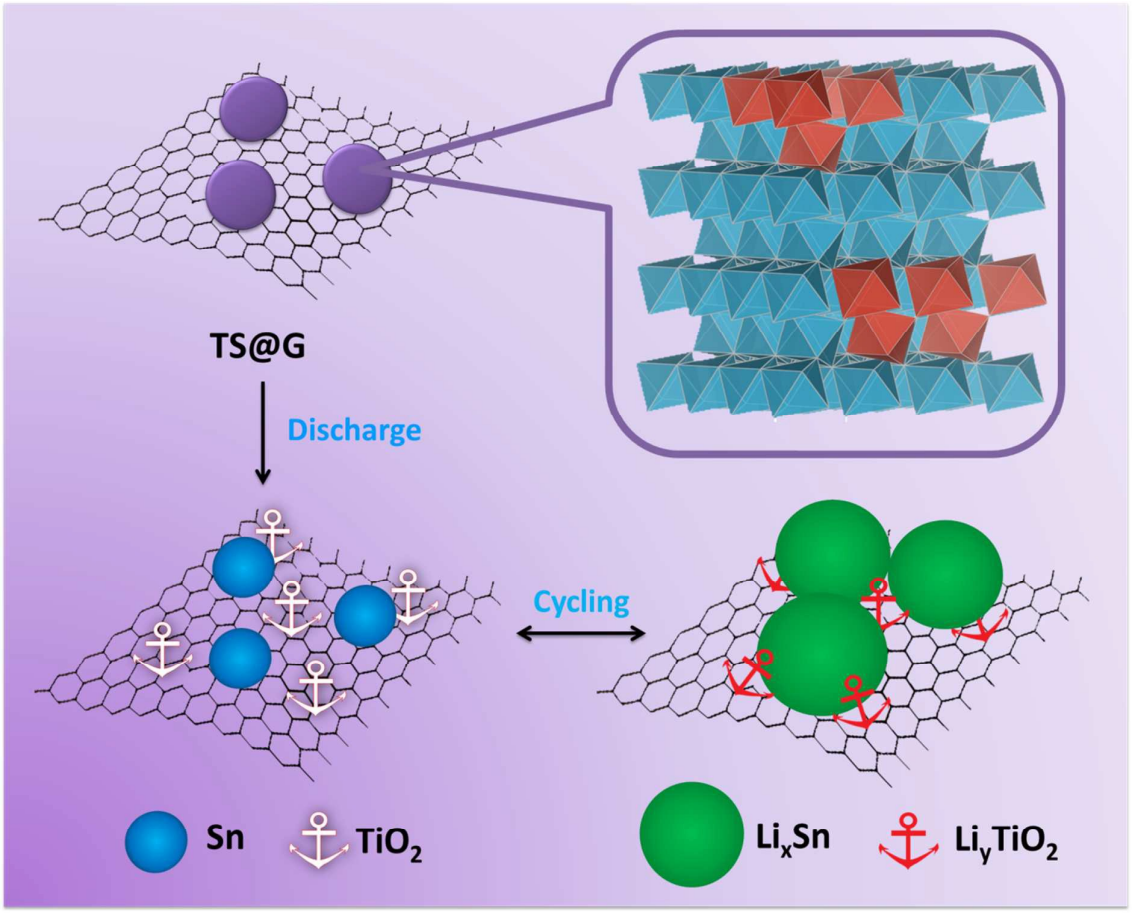

Journal Name RSCPublishing

ARTICLE

Anchoring Ultra-fine TiO_2-SnO_2 Solid Solution Particles onto Graphene by One-Pot Ball-Milling for Long-life Lithium-ion Batteries

Cite this: DOI: 10.1039/x0xx00000x

Received 00th January 2012,
Accepted 00th January 2012

DOI: 10.1039/x0xx00000x

www.rsc.org/

Sheng Li[a], Min Ling[a], Jingxia Qiu[a], Jisheng Han[b], and Shanqing Zhang[a] *,

A low cost, up-scalable and one-pot wet-mechanochemical approach is designed for fabricating TiO_2-SnO_2@graphene nanocomposites where TiO_2 and SnO_2 solid solution nanoparticles are evenly anchored on graphene sheets. As an anode material of lithium ion batteries (LIBs), the as-prepared nanocomposites deliver superior rate performance of 388 mAh g^{-1} at 1.5 A g^{-1} and outstanding reversible cycling stability (617 mAh g^{-1} at 0.4 A g^{-1} after 750 cycles, 92.2% capacity retention), due to the synergistic effects contributed from individual components, i.e.,: high specific capacity of SnO_2, excellent conductivity of 3D porous graphene networks, good rate capability and structural stability of TiO_2 structure.

Introduction

Rechargeable lithium ion batteries (LIBs) have been the dominant choice for almost all portable devices. To meet the increasing demands of future energy storage devices including electrical vehicles (EVs) and smart electricity grids, low cost, high rate and long life properties of the rechargeable batteries are highly desirable. [1, 2]. Due to significantly higher theoretical capacity and safety in comparison with conventional graphite anode, many metal oxides and their composites, such as SnO_2, TiO_2, Fe_2O_3, and CoO, etc., have been extensively investigated [3-7]. Among them, SnO_2 is one of the most promising materials because of its high theoretical specific capacity (782 mAh g^{-1}) [8-12]. However, severe volume expansion/contraction (>300%) of the SnO_2 electrode during charge/discharge processes would result in electrode pulverization, leading to short life time [13]. Besides, poor electrical conductivity and ions transportability also limits the practical rate capability and consequently hinder the material from commercial high power applications such as electric vehicles.

It is well established that TiO_2 delivers excellent rate capabilities with trivial volume change (<4%) during charge/discharge processes for TiO_2 due to its inherent structural robustness and intercalation mechanism [14]. In order to overcome the stability problems of SnO_2, TiO_2 is proposed to support SnO_2 to build robust retaining structures to accommodate the dramatic volume change of SnO_2 electrodes. Fortunately, the similarity of Ti^{4+} and Sn^{4+} in size and the matching crystal lattices of rutile TiO_2 and SnO_2 make possible the formation of hybrid structures. Numerous hybrid structures, such as $Ti_xSn_{1-x}O_3$ solid solution [15], (Sn-Ti)O_2 nanocomposites [16], $Ti_{2/3}Sn_{1/3}O_2$ [17], Ti(IV)/Sn(II) co-doped SnO_2 nanosheets [18], tin titanate Nanotubes [19], mesoporous Sn-doped TiO_2 thin films [20], coaxial SnO_2@TiO_2 nanotube hybrids [21] and TiO_2-supported-SnO_2 [22] were investigated for application in LIBs in recent years. However, there are still a significant room to be improved in terms of power and stability.

Graphene has been well-considered as an effective addictive for the electrochemical performance improvement of LIBs electrodes due to its unique 2-D structure, large surface area, excellent electronic conductivity and resilient mechanical properties[23-25]. The incorporation of graphene and metal oxides can also address the nanoparticle aggregation during electrode preparation, improve and maintain the conductivity and alleviate electrode pulverization during charge/discharge process. It has been demonstrated that graphene enhance the cycle stability and rate capacity for SnO_2 based anodes [13, 26, 27]. Basing on the aforementioned findings, we propose to tackle the problems by collectively utilizing the inherent functions of the TiO_2, SnO_2 and graphene. Exceptional electrochemical performances can be expected if the functions of the individual component can be synergistically incorporated, including the high specific capacity of SnO_2, excellent conductivity of graphene, excellent rate capability and structural configuration of TiO_2.

The quality and the manufacturing cost of the electrode materials determine the performance and competiveness of the resultant batteries, respectively. Up to now, the syntheses of

TiO_2/SnO_2 and graphene hybrid materials involve multi-stepped and complicated processes with poor production yield and limited improvements in electrochemical performance. In this work, we develop a one-pot wet-mechanochemical method (i.e., wet ball-milling) to synthesize ultra-fine TiO_2-SnO_2@graphene composite (TS@G), where Ti-doped SnO_2 nanoparticles are anchored evenly and tightly on the graphene sheets. This wet mechanochemical method is simple, fast, facile, most importantly, up-scalable and therefore low manufacturing cost.

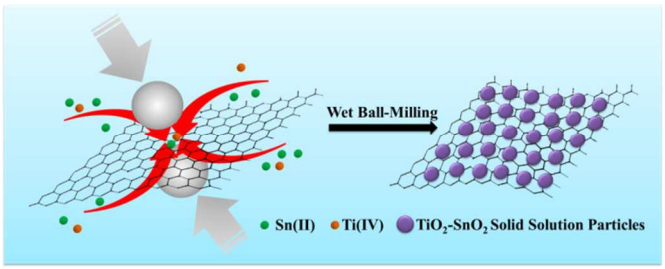

Scheme. 1. Schematic representation of the formation process of TS@G nanocomposites via the wet ball-milling route.

$TiOSO_4$ and $SnCl_2$ and graphene oxides (GO) are used as precursors for the synthesis. They are firstly hydrolysed to $TiO(OH)_2$ and Sn(OH)Cl [13, 28], and homogeneously dispersing in water, respectively. Sn(OH)Cl is a moderate reductant that is capable of reducing GO under wet ball-milling conditions.[13, 29]. The aqueous environment could help homogeneous distributions of these intermediates and precursors and subsequently facilitate the formation of the ultra-fine size for the product particles. As shown in Scheme 1, the impacts from the powerful ball-collisions during the process would direct these particles and precursors together at collision points, where collision-induced energy triggers and/or accelerates the reactions, i.e., GO is reduced by Sn(II). Owing to the matching lattice of rutile crystal structure of TiO_2 and SnO_2, TiO_2-SnO_2 solid solutions could be thermodynamically-favourable created in this process [16, 30]. Most significant of all, the resultant TiO_2-SnO_2 solid solution particles would be tightly and evenly anchored on reduced graphene sheets surfaces. Conductive porous networks are therefore built along 3D graphene skeletons. As a result, TiO_2-SnO_2 solid solution anchored on graphene nanocomposite (TS@G) is synthesised and overall chemical processes can be represented by Eqn. 1 and 2:

$$SnCl_2 + H_2O \leftrightarrow Sn(OH)Cl + HCl \quad (1)$$

$$Ti(IV) + Sn(II) + GO \xrightarrow{Wet\ Ball-Milling} TS@G \quad (2)$$

The composites are applied as anode material of LIBs in this work. In initial charge/discharge process, the TiO_2-SnO_2 solid solution particles are subject to lithium-ion intercalation process at TiO_2 lattice while SnO_2 is reduced to Sn particles. It is expected that for TS@G composite, the rate capacity could be significantly enhanced by the conductivity of graphene and the fast insertion/extraction abilities of TiO_2 for Li-ions [4]; the TiO_2 as well as the 3-D graphene network could confine SnO_2 and resultant Sn particles, alleviating the influence of the drastic volume change and preventing the Sn particles from aggregation and electrode from pulverisation.

Experimental Section

Material Preparation

$SnCl_2$•$2H_2O$ (0.45 g, Merck Pty. Ltd.), $TiOSO_4$•xH_2O (0.03 g, chemical, Ti basis as $TiO_2 \geq 29$ wt%, Sigma-Aldrich) and graphene oxide (GO, 0.1 g, Tianjin Plannano Technology Co. Ltd.) are firstly dispersed in 10 mL deionized water. The resultant mixture is added to a planetary zirconia ball miller at room temperature at a speed of 500 rpm for 3 h. Then the as-prepared product TS@G is washed in water and ethanol in sequence, and subsequently dried in a vacuum oven at 60 °C. SnO_2@graphene (S@G) sample is prepared in same condition only without any Ti sources.

Material Characterizations

The microstructure and morphology of materials were examined by scanning electron microscope (SEM, JSM-7001F) and transmission electron microscopy (TEM) (FEI Model Tecnai G20). Energy-dispersive X-ray spectroscopy (EDS) analysis and element mapping were obtained from JEOL JSM-6610. The multipoint Brunauer–Emmett–Teller (BET) surface area was estimated using adsorption data obtained from a surface area analyser (Micromeritics Tristar 3020). X-ray diffraction (XRD) was characterized (Model LabX-6000, Shimadzu, Japan) using CuKα radiation at 40 kV and 40 mA over the 2θ range of 10~80 °. For X-ray photoelectron spectroscopy (XPS, Kratos Axis ULTRA incorporating a 165 mm hemispherical electron energy analyzer) test, all binding energies were referenced to the C 1s peak (284.8 eV).

Electrochemical measurements

As active materials, the samples are mixed with 10 wt % carbon black and 10 wt% polyvinylidene difluoride (PVDF, Aldrich) in N-methyl-2-pyrrolidone (NMP, Aldrich) solvent to form homogeneous slurries. The resultant slurries are uniformly coated onto Cu foils with an area of 1 cm^2. The loading of the electrode material is c.a. 2 mg. The pasted Cu foils are dried in a vacuum oven at 60 °C and then pressed by a double-roll compressor. CR2032 coin-type cells are assembled in an argon-filled M-Braun glove box. A porous polypropylene film was used as the separator, a lithium sheet as the counter electrode, and 1 M $LiPF_6$ in a 1:1 (w/w) mixture of ethylene carbonate (EC) and dimethyl carbonate (DMC) as the electrolyte. To measure the electrochemical capacity and cycle life of the working electrodes, the cells are charged and discharged using LANDCT 2001A battery tester (Wuhan, PRC) in a voltage range from 0.01 to 2.5 V vs Li/Li^+. Cyclic voltammograms (CVs) were performed using a CHI 660D electrochemical workstation (CH Instrument, Shanghai, PRC). CVs were recorded between 2.5 V and 0.01 V at a scan rate of 0.1 mV s^{-1},

using the composite as the working electrode and a lithium sheet as both counter electrode and reference electrode. Electrochemical impedance spectroscopy (EIS) was also carried out in this two electrodes system with amplitude of 5 mV over the frequency range from 100 kHz to 0.01 Hz.

Results and discussion

After the precursors are dispersed into the water solution, light brown colour slurry is obtained. The colour is originated from GO. The 3h ball-milling process turns it into pure a dark-black slurry, suggesting that GO is reduced to graphene. The quantitative elemental analysis from EDS shows the atomic ratio of Ti: Sn of the composite is c.a. 1:14 which is consistent with the initial ratio (*c.a.* 1:15). The morphologies investigation by SEM in Fig. 1 shows that GO possesses a semi-transparent and sheet-like morphology (Fig. 1a and 1b). After the wet ball-milling process, the graphene sheets become significantly thicker due to the resultant TiO_2-SnO_2 solid solution particles are evenly anchored onto the graphene sheets (Fig. 1c and 1d). The size of the graphene sheets is well maintained at c.a. 1~10 μm. The EDS mapping (Fig. 2) also illustrates that Sn and Ti elements are evenly distributed on the graphene planes.

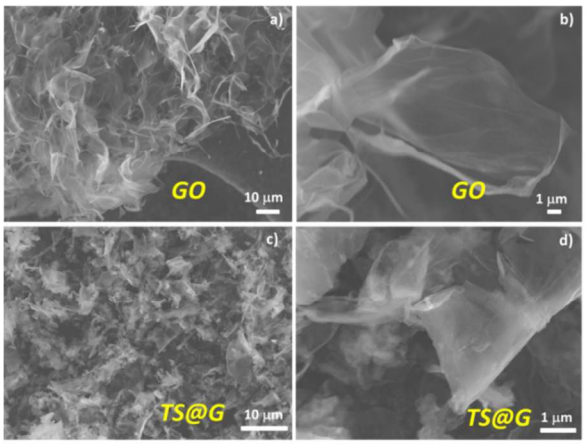

Fig. 1. SEM images of the GO (a, b) and TS@G (c, d) under different magnifications.

The TEM images (Fig. 3) further confirm that the metal oxides nanoparticles are anchored on the surface of graphene uniformly in the wet ball-milling process. TiO_2-SnO_2 solid solutions are ultra-fine particles with an average size of *c.a.* 3 nm as measured in HR-TEM image (Fig. 3c). Commonly, the products from ball-milling method are much larger in size due to the inherent limitation of ball-milling process and the aggregation of the powders, typically 100 nm[31]. In this case, the unexpected ultrafine size of TS@G could be attributed to the adoption of the aqueous reaction media and the effective fixation of the resultant nanoparticles onto the graphene planes. The former helps the distribution of precursors in the entire reaction media while the latter prohibits the mobility of the resultant nanoparticles and subsequent growth or merging of the nanoparticles. Fringes for (110) planes of TiO_2-SnO_2 solid solution crystals shows that the distance between planes is c.a. 0.34 nm. In the SAED pattern for TS@G in Fig. 3b, inset, sixfold symmetric diffraction spots can be correspondent to the graphene sheet [32, 33], while a series of concentric circles are resulted from electron diffraction of (100), (101), and (211) planes of the crystal. These observations imply the successful anchoring of TS nanoparticles on graphene sheets.

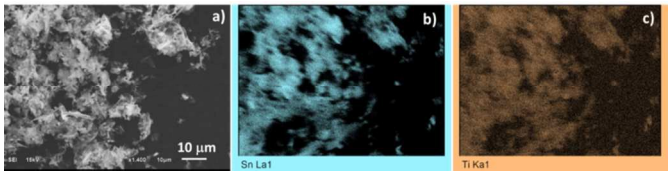

Fig. 2. SEM image (a), corresponding EDS mapping images for Sn (b), and Ti (c) of the TS@G.

In Fig. 3d, the pore size distribution derived from the N_2 adsorption/desorption isotherm indicates mesoporous structure with wide pore size distribution. For the large mesopores (> 10 nm), the N_2 adsorption/desorption isotherm illustrates type II and have a sharp increase at the high relative pressure region [34]. These mesopores could be resulted from the 3D graphene structure constructed by TS@G sheets as shown in Fig. 1c. The substantial amount of mesoporous (*c.a.* 3nm) could be attributed to the nanostructure assembled by the ultrafine TiO_2-SnO_2 solution nanoparticles in the 3D graphene structure. As a result, a large surface area of 214 m^2/g is obtained. It is well-established that such a porous structure could provide excessive contacts between the electrode material and the electrolyte, enhancing mass transport of lithium-ions in charge/discharge process, which is crucial to rate capability of LIBs.

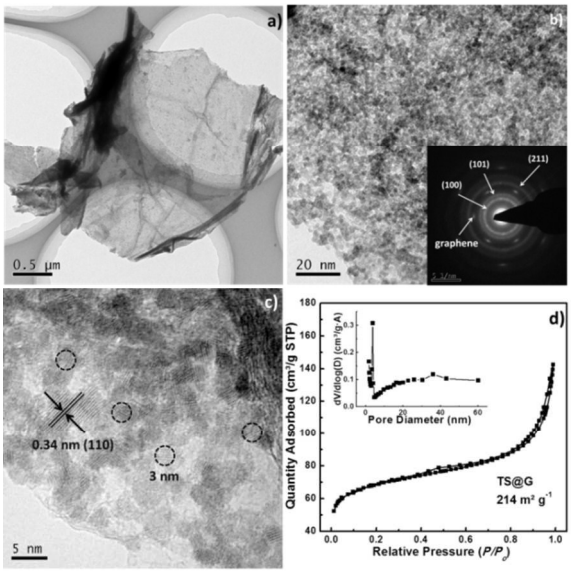

Fig. 3. TEM images of different magnifications (a, b), corresponding SAED image (inset, b) of the TS@G sample, HRTEM image (c) and BET N_2 adsorption/desorption isotherms for TS@G (d).

XRD profiles for both the S@G and TS@G nanocomposites are shown in Fig. 4a. Though similar profiles of SnO_2 crystal

are observed for both samples (JCPDS PDF file: 41-1445), it can be observed that the TS@G profile is shifted slightly to a large angle direction. This can be explained by the fact that Ti^{4+} (0.68Å) are slightly smaller than Sn^{4+} (0.71Å) and for the product, a more compact crystal structure with reduced lattice parameters are obtained. According to Bragg's Equation[35], and data presented in Fig. 4b, the distance value (*d*) for (211) planes is changed from 0.180 nm of the sample S@G to 0.176 nm of the sample TS@G.

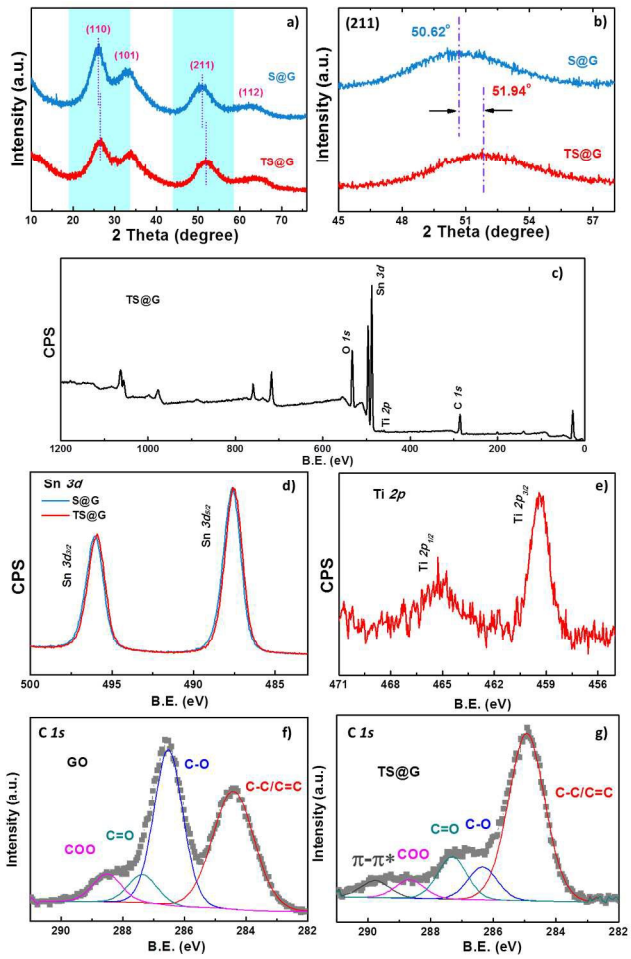

Fig. 4. XRD patterns of the S@G and TS@G composites (a, b); XPS survey spectra of the TS@G (c); Sn 3d XPS spectra of the S@G and TS@G (d), Ti 2p XPS spectra of TS@G (e) and C 1s spectra for GO (f) and TS@G (g).

XPS tests are conducted to evaluate the valence states for the TS@G sample. A general survey pattern in Fig. 4c demonstrates the presence of elements O, C, Sn and Ti. The carbon content can be controlled by adjusting the ratio of precursors since no carbon loss in the synthesis process. The graphene weight percentage here is measured and calculated from the spectra, and it is as *c.a.* 23%. High resolution of Sn *3d* and Ti *2p* XPS spectra are displayed in Fig. 4d and Fig. 4e, respectively. Two Sn *3d* peaks including Sn $3d_{3/2}$ at 495.9 eV and Sn $3d_{5/2}$ at 487.5 eV, suggest the formation of Sn^{4+} [13, 36]. Interestingly, the binding energy of Ti 2p peaks (Ti $2p_{1/2}$ at 465.3 eV and Ti $2p_{3/2}$ at 459.4 eV) are *c.a.* 1 eV higher than normal TiO_2 in the literature[4], which is owing to the loss of electrons from Ti to Sn and graphene[27], further confirming the formation of TS@G composites and the strong bonding between the nanoparticles on graphene sheets. For C *1s* XPS spectra, in comparison of GO (Fig. 4f), the intensities of the peaks of carbon oxygen functional groups for TS@G (Fig. 4f) decrease dramatically, indicating a successfully reduction of graphene oxide.

The electrochemical characteristics for commercial SnO_2 nanopowders, S@G and TS@G electrodes are firstly tested by EIS measurements. The Nyquist plots in Fig. 5a displays semi-cycles in high and middle frequency region that are related to the charge transfer resistances (R_{ct}); while inclined lines in the low frequency region are ascribed to Warburg impedance. Compared with the R_{ct} of the commercial SnO_2 nanopowders (464 Ω), the R_{ct} values of S@G (192 Ω) and TS@G (87 Ω) are much smaller, which can be ascribed to the incorporation of graphene. Furthermore, the lower resistance of TS@G than S@G suggests that SnO_2 and TiO_2 are well-incorporated with each other which facilitates interfacial electron transfer due to the matching lattice of SnO_2 and TiO_2[27].

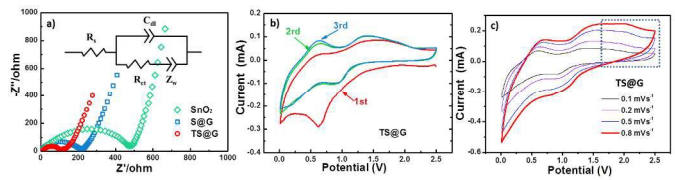

Fig. 5. Nyquist plots of the electrodes for commercial SnO_2, S@G and TS@G samples (a); CV curves for the TS@G sample for the first 3 cycles (b); CV curves for TS@G at various scan rates (c).

The CV curves for TS@G for the first 3 cycles are shown in Fig. 5b. Two broad cathodic peaks at 0.65 V and 0.01 V can be observed for the first cycle, corresponding to the formation of solid electrolyte interface (SEI) layer, the partial reversibility of the reduction of SnO_2 to Sn, and the formation of Li_2O as shown in Eqn 3 [37]. From the second cycle, the CV curves are overlapped, suggesting the stabilization of electrode reaction and a good reversibility. Two characteristic redox pairs at potentials of (1.0 V and 1.3 V) and (0.01 V and 0.6 V) are corresponding to the reduction of SnO_2 and the formation of Li_xSn alloys (Eqn. 4), respectively. This is consistent with the observation of normal S@G electrode[13]. However, when the scan rate increases, an additional anodic peak could be observed at 2.1 V for TS@G, as shown in Fig. 5c. The extra anodic peak is a typical behaviour for the diffusion of lithium ions into TiO_2 structures, suggesting that the titanium oxides in TS@G undergo lithium-ion intercalation process (see Eqn 5). These could also be further evidenced by XRD pattern for TS@G electrode after lithium insertion (Fig. 6).

$$SnO_2 + 4Li^+ + 4e^- \rightarrow Sn + 2Li_2O \quad (3)$$

$$Sn + xLi^+ + xe^- \leftrightarrow Li_xSn \ (0 \le x \le 4.4) \quad (4)$$

$$TiO_z + yLi^+ + xe^- \leftrightarrow Li_yTiO_z \quad (5)$$

At higher scan rates, titanium oxides contribute more rates cycling ability, leading to outstanding overall rate capacity for the electrodes. It not only provides more reaction active sites for lithium ions, but might also contribute pseudocapacitance to the total capacity for the defective structure and the adsorption of lithium ions.

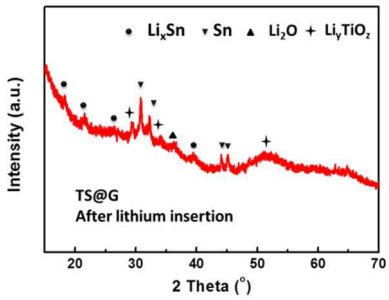

Fig. 6. XRD pattern of the TS@G electrode after lithium insertion (the 3rd cycle).

The battery performances are investigated by galvanostatic charge/discharge measurements. Fig. 7a shows rate capacities at different specific current densities: for TS@G sample, specific capacities of 790 mAh g^{-1}, 682 mAh g^{-1}, 600 mAh g^{-1}, 481 mAh g^{-1}, and 388 mAh g^{-1} are obtained at 0.1 A g^{-1}, 0.25 A g^{-1}, 0.5 A g^{-1}, 1 A g^{-1} and 1.5 A g^{-1} TS@G, respectively, which are much higher than corresponding specific capacities of S@G. It is notable that after 50 cycles, when the specific current is set back to 0.1 A g^{-1}, the specific capacity of TS@G goes up back to 767 mAh g^{-1}, indicating excellent rate cycling property.

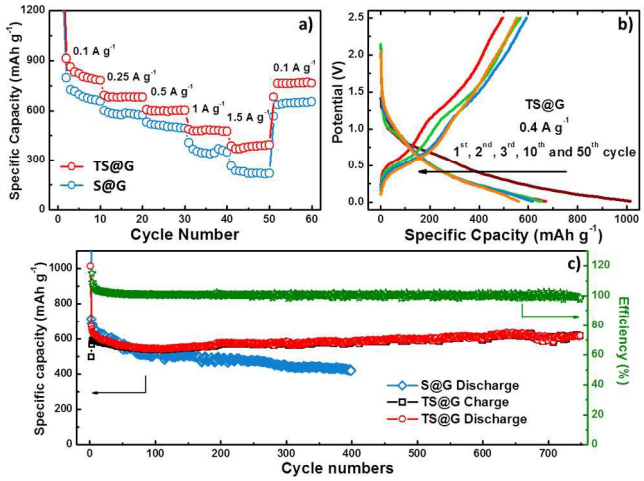

Fig. 7. The rate capacities profiles from 0.1 to 1.5 A g^{-1} for S@G and TS@G samples (a); the 1st, 2nd, 3rd, 10th and 50th cycle charge/discharge profiles for TS@G at a current density of 0.4 A g^{-1} in the voltage range 0.01-2.5 V (b); cycling ability for S@G and TS@G samples at 0.4 A g^{-1} and coulombic efficiency profile for TS@G (c).

Fig. 7b displays the charge/discharge curves for TS@G at 0.4 A g^{-1} for the 1st, 2nd, 3rd, 10th and 50th cycle. The discharge capacity reaches 1013 mAh g^{-1} for the first cycle and stabilized at 670 mAh g-1 from the second cycle. The decay of the capacity is due to the irreversible reaction for SEI film formation on the surface of network structure of the electrode materials. From the 2nd cycle, the shapes of discharge curves do not change, indicating the stabilization of the reversible electrochemical reactions. It is notable that the TS@G achieves an outstanding cycling long life performance as demonstrated in Fig. 7c (under a current density of 0.4 A g^{-1}). Even after 750 cycles, the specific capacity is maintained over 617 mAh g^{-1}, i.e., 92.2% capacity retention comparing with the 2nd cycle. These electrochemical performances are among the best of the state-of-the-art TiO_2/SnO_2 electrodes for LIBs (as shown in Table 1)[15-20, 26, 27]. The columbic efficiency of the TS@G electrode can be kept at *c.a.* 100% for the entire charge/discharge processes, confirming the excellent reversibility of the electrode. In comparison, the capacity of S@G electrode drops to 420 mAh g^{-1} after 400 cycles.

Table 1 LIBs performances comparison for the TS@G sample versus state-of-the-art TiO_2/SnO_2 graphene composite materials.

Materials	Rate current densities	Rate Specific capacity	Cycling current density	Cycling specific capacity (cycle numbers)	Ref.
TiO_2-SnO_2@graohene (TS@G)	1 A g^{-1} 1.5 A g^{-1}	481 mAh g^{-1} 388 mAh g^{-1}	0.4 A g^{-1}	617 mAh g^{-1} (750 cycles)	This work
$Ti_xSn_{1-x}O_3$ solid solution	-	-	0.2 mA cm^{-2}	506 mAh g^{-1} (30 cycles)	[13]
(Sn-Ti)O_2 nanocomposites	1.5 A g^{-1} 3 A g^{-1}	~210 mAh g^{-1} ~190 mAh g^{-1}	0.03 A g^{-1}	318.6 mAh g^{-1} (50 cycles)	[14]
Nanocrystalline $Ti_{2/3}Sn_{1/3}O_2$	0.76 A g^{-1} 7.56 A g^{-1}	~100 mAh g^{-1} ~20 mAh g^{-1}	18.9 mA g^{-1}	300 mAh g^{-1} (100 cycles)	[15]
Graphene-based TiO_2/SnO_2 hybrid nanosheets	1.6 A g^{-1} 4 A g^{-1}	400 mAh g^{-1} 260 mAh g^{-1}	1.6 A g^{-1}	600 mAh g^{-1} (300 cycles)	[25]
Ti(IV)/Sn(II) co-doped SnO_2 nanosheets	-	-	0.25 A g^{-1}	319 mAh g^{-1} (35 cycles)	[16]
Tin Titanate Nanotubes	1 A g^{-1}	225 mAh g^{-1}	0.25 A g^{-1}	300 mAh g^{-1} (300 cycles)	[17]
Graphene–TiO_2–SnO_2 ternary nanocomposites	1 A g^{-1}	250 mAh g^{-1}	0.05 A g^{-1}	537 mAh g^{-1} (50 cycles)	[24]
Mesoporous Sn-doped TiO_2 thin films	0.168 A g^{-1}	153 mAh g^{-1}	0.084 A g^{-1}	252.5 mAh g^{-1} (80 cycles)	[18]

The mechanisms responsible for the superior performance in rate capability and stability of the TS@G electrode can be summarised in Scheme 2: firstly, the one-pot ball-milling process facilitates the formation of TiO_2-SnO_2 solid solution particles. Secondly, after the first cycle for the battery, the solid solution nanoparticles are converted into to TiO_2 and metal Sn

particles via chemical processes of Eqns (3-5), respectively. Thirdly and most importantly, TiO_2 nanoparticles that strongly mounted onto the graphene sheets due to the "Ti-O-C" bonding [14] can act as "anchors" to retain the Sn particles in the confined areas and physically connect the Sn particles and graphene sheets together. In this way, Sn particles will maintain good contact with the TiO_2 and graphene regardless of the dramatic volume expansion or shrinkage of Li_xSn particles. It is to note this effect can be realized only when ultra-fine size (of TiO_2 and SnO_2 solid solution particles) and homogenous distribution of TiO_2 and SnO_2 are achieved since excessive volume expansion of large Sn particles could physically destroy the conductive porous structure. The anchoring function for the TiO_2 nanoparticles also prevents the restacking of graphene and the aggregations of Sn particles during charge/discharge processes due to TiO_2 are robust and do not undergo volume changes. In Scheme 2, the hollow anchors represent the delithiated TiO_2 while the red solid anchors stand for lithiated TiO_2 particles. The TiO_2 "anchors" could provide a unique mechanism to maintain the robust, conductive and porous structure for Sn alloying/dealloying processes, facilitating electron conductivity as well as lithium-ion conductivity; lastly, these TiO_2 "anchors" undergo lithium-ion intercalation process while Sn particles carry out lithium alloying process. TiO_2 contributes significantly in high rate capability in this circumstance [4]. This process further improves the rate capabilities. Finally, the aforementioned mechanisms provide an effective platform to graphene to fulfil the primary roles in the enhancement of electronic conductivity, surface area and mechanical strength.

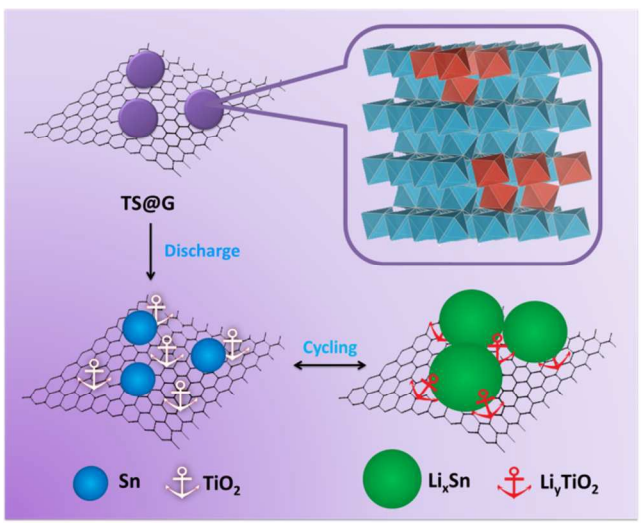

Scheme. 2. The schematic representation of charge/discharge cycle stability for TS@G electrode.

Conclusions

TS@G composites have been successfully synthesized by a facile one-pot wet mechanochemical method. In the composites, the in-situ formed ultra-fine TiO_2-SnO_2 solid solution particles are strongly anchored onto the graphene plane, resulting in conductive and robust structure. TiO_2 particles realize dual functions in this scenario: on the one hand, they acts as strong "anchors" to physically confine Sn particles in place, securing Sn and graphene sheet together in the charge/discharge process; on the other hand, the TiO_2 particles also contribute to rate capability. Consequently, the TS@G nanocomposite delivers exceptional rate capability (388 mAh g^{-1} at 1.5 A g^{-1}) and an outstanding long cycle life (617 mAh g^{-1}, 92.2% capacity retention after 750 cycles, 0.4 A g^{-1}). This work suggests that wet-mechanochemical route could be a very promising strategy for manufacturing low cost and high quality electrode materials for LIBs industry.

Acknowledgements

The authors acknowledge the financial supports from Australia Research Council and Griffith University, Australia, and the facilities and the scientific and technical assistance of the Australian Microscopy & Microanalysis Research Facility at the Centre for Microscopy and Microanalysis (CMM) at the University of Queensland, Australia.

Notes and references

[a] Centre for Clean Environment and Energy, Environmental Futures Research Institute, and Griffith School of Environment, Griffith University, Gold Coast, QLD 4222, Australia
[b] Queensland Micro- and Nanotechnology Centre, Griffith University, Brisbane, QLD 4111, Australia
Email address: s.zhang@griffith.edu.au

† Footnotes should appear here. These might include comments relevant to but not central to the matter under discussion, limited experimental and spectral data, and crystallographic data.
Electronic Supplementary Information (ESI) available: [details of any supplementary information available should be included here]. See DOI: 10.1039/b000000x/

1. J. Qiu, C. Lai, E. Gray, S. Li, S. Qiu, E. Strounina, C. Sun, H. Zhao and S. Zhang, *J. Mater. Chem. A*, 2014, **2**, 6353.
2. M. Ling, J. Qiu, S. Li, G. Liu and S. Zhang, *J. Mater. Chem. A*, 2013, **1**, 11543.
3. J. Qiu, P. Zhang, M. Ling, S. Li, P. Liu, H. Zhao and S. Zhang, *ACS Appl. Mater. Interfaces*, 2012, **4**, 3636−3642.
4. J. Qiu, S. Li, E. Gray, H. Liu, Q.-F. Gu, C. Sun, C. Lai, H. Zhao and S. Zhang, *J. Phys. Chem. C*, 2014, **118**, 8824.
5. M. V. Reddy, G. V. Subba Rao and B. V. Chowdari, *Chem. Rev.*, 2013, **113**, 5364.
6. X. Huang, R. Wang, D. Xu, Z. Wang, H. Wang, J. Xu, Z. Wu, Q. Liu, Y. Zhang and X. Zhang, *Adv. Funct. Mater.*, 2013, **23**, 4345.
7. X. Wang, Q. Xiang, B. Liu, L. Wang, T. Luo, D. Chen and G. Shen, *Sci. Rep.*, 2013, **3**, 2007.
8. D. Wang, X. Li, J. Wang, J. Yang, D. Geng, R. Li, M. Cai, T.-K. Sham and X. Sun, *J. Phys. Chem. C*, 2012, **116**, 22149.
9. J. S. Chen and X. W. Lou, *Small*, 2013, **9**, 1877.

10. C. Zhang, X. Peng, Z. Guo, C. Cai, Z. Chen, D. Wexler, S. Li and H. Liu, *Carbon*, 2012, **50**, 1897.
11. C. Gu, H. Zhang, X. Wang and J. Tu, *Mater. Res. Bull.*, 2013, **48**, 4112.
12. C. D. Gu, Y. J. Mai, J. P. Zhou, Y. H. You and J. P. Tu, *J. Power Sources*, 2012, **214**, 200.
13. S. Li, Y. Wang, C. Lai, J. Qiu, M. Ling, W. N. Martens, H. Zhao and S. Zhang, *J. Mater. Chem. A*, 2014, 10211.
14. J. Qiu, C. Lai, Y. Wang, S. Li and S. Zhang, *Chem. Eng. J.*, 2014, **256**, 247.
15. J. Yan, H. Song, H. Zhang, J. Yan, X. Chen, F. Wang, H. Yang and M. Gomi, *Electrochim. Acta*, 2012, **72**, 186.
16. C.-C. Chang, Y.-C. Chen, C.-W. Huang, Y. H. Su and C.-C. Hu, *Electrochim. Acta*, 2013, **99**, 69.
17. I. Issac, M. Scheuermann, S. M. Becker, E. G. Bardají, C. Adelhelm, D. Wang, C. Kübel and S. Indris, *J. Power Sources*, 2011, **196**, 9689.
18. H. Wang, L. Xi, J. Tucek, Y. Zhan, T. F. Hung, S. V. Kershaw, R. Zboril, C. Y. Chung and A. L. Rogach, *Nanoscale*, 2013, **5**, 9101.
19. H. Wang, L. Xi, J. Tucek, C. Ma, G. Yang, M. K. H. Leung, R. Zboril, C. Niu and A. L. Rogach, *ChemElectroChem*, 2014, **1**, 1563.
20. Y. Wang, M. Xu, Z. Peng and G. Zheng, *J. Mater. Chem. A*, 2013, **1**, 13222.
21. X. Wu, S. Zhang, L. Wang, Z. Du, H. Fang, Y. Ling and Z. Huang, *J. Mater. Chem.*, 2012, **22**, 11151.
22. Y.-M. Lin, R. K. Nagarale, K. C. Klavetter, A. Heller and C. B. Mullins, *J. Mater. Chem.*, 2012, **22**, 11134.
23. J. Zhu, D. Wang, T. Liu and C. Guo, *Electrochim. Acta*, 2014, **125**, 347.
24. X. Zhou, L. J. Wan and Y. G. Guo, *Adv. Mater.*, 2013, **25**, 2152.
25. J. Zhu, D. Yang, Z. Yin, Q. Yan and H. Zhang, *Small*, 2014, **10**, 3480.
26. X. Jiang, X. Yang, Y. Zhu, K. Fan, P. Zhao and C. Li, *New J. Chem.*, 2013, **37**, 3671.
27. Y. Tang, D. Wu, S. Chen, F. Zhang, J. Jia and X. Feng, *Energy Environ. Sci.*, 2013, **6**, 2447.
28. K. Akiyama, N. Toyama, K. Muraoka and M. Tsunashima, *J. Am. Ceram. Soc.*, 1998, **81**, 1071.
29. S. Li, Y. Wang, J. Qiu, M. Ling, H. Wang, W. Martens and S. Zhang, *RSC Adv.*, 2014, **4**, 50148.
30. H. Uchiyama, E. Hosono, H. Zhou and H. Imai, *Solid State Ionics*, 2009, **180**, 956.
31. C. Lai, Z. Wu, Y. Zhu, Q. Wu, L. Li and C. Wang, *J. Power Sources*, 2013, **226**, 71.
32. H. Zhou, W. J. Yu, L. Liu, R. Cheng, Y. Chen, X. Huang, Y. Liu, Y. Wang, Y. Huang and X. Duan, *Nat. Commun.*, 2013, **4**, 2096.
33. C. Wang, W. Chen, C. Han, G. Wang, B. Tang, C. Tang, Y. Wang, W. Zou, W. Chen, X.-A. Zhang, S. Qin, S. Chang and L. Wang, *Sci. Rep.*, 2014, **4**, 4537.
34. Y. Li, H. Zhang, Y. Wang, P. Liu, H. Yang, X. Yao, D. Wang, Z. Tang and H. Zhao, *Energy Environ. Sci.*, 2014, **7**, 3720.
35. W. L. Bond, *Acta Crystallogr.*, 1960, **13**, 814.
36. S. Li, J. Qiu, M. Ling, F. Peng, B. Wood and S. Zhang, *ACS Appl. Mater. Interfaces*, 2013, **5**, 11129.
37. P. Wu, N. Du, H. Zhang, C. Zhai and D. Yang, *ACS Appl. Mater. Interfaces*, 2011, **3**, 1946.